JACS
JOURNAL OF THE AMERICAN CHEMICAL SOCIETY
ARTICLE
pubs.acs.org/JACS

Kinetic Mechanisms in Morpholino−DNA Surface Hybridization

Yatao Liu, Damion Irving, Wanqiong Qiao, Dongbiao Ge, and Rastislav Levicky*

Department of Chemical and Biological Engineering, Polytechnic Institute of New York University, 6 MetroTech Center, Brooklyn, New York 11201, United States

S *Supporting Information*

ABSTRACT: Morpholinos (MOs) are DNA analogues whose uncharged nature can bring fundamental advantages to surface hybridization technologies such as DNA microarrays, by using MOs as the immobilized, or "probe", species. Advancement of MO-based diagnostics, however, is challenged by limited understanding of the surface organization of MO molecules and of how this organization impacts hybridization kinetics and thermodynamics. The present study focuses on hybridization kinetics between monolayers of MO probes and DNA targets as a function of the instantaneous extent of hybridization (i.e., duplex coverage), total probe coverage, and ionic strength. Intriguingly, these experiments reveal distinct kinetic stages, none of which are consistent with Langmuir kinetics. The initial stage, in which duplex coverage remains relatively sparse, indicates confluence of two effects: blockage of target access to unhybridized probes by previously formed duplexes and deactivation of the solid support due to consumption of probe molecules. This interpretation is consistent with a surface organization in which unhybridized MO probes localize near the solid support, underneath a layer of MO−DNA duplexes. As duplex coverage builds, provided saturation is not reached first, the initial stage can transition to an unusual regime characterized by near independence of hybridization rate on duplex coverage, followed by a prolonged approach to equilibrium. The possible origins of these more complex latter behaviors are discussed. Comparison with published data for DNA and peptide nucleic acid (PNA) probes is carried out to look for universal trends in kinetics. This comparison reveals qualitative similarities when comparable surface organization of probes is expected. In addition, MO monolayers are found capable of a broad range of reactivities that span reported values for PNA and DNA probes.

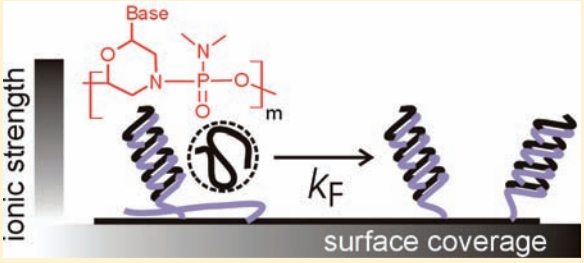

1. INTRODUCTION

Morpholinos (MOs), a class of uncharged DNA mimics,[1] are capturing increasing interest for diagnostic applications[2−7] in addition to more established uses in gene knockdown.[1,8] Because thermodynamics of MO−DNA interactions are different from those between two DNA strands,[8,9] under suitable conditions MOs can favor formation of signal-producing MO−DNA associations over competing interactions between sample nucleic acid sequences.[8] In addition, MOs' lack of charge makes them especially useful for electrostatic transduction; indeed, the assays reported to date have in one way or another relied on electrostatics.[2−7] These assays have been performed on solid supports on which immobilized MO "probes" react with analyte "targets" from solution. A key motivation for use of solid supports is their capacity for high-throughput multiplexing.[10]

Hybridization on solid supports is considerably more complex than in solution because of additional interactions that arise from the support and from the high concentration of probe molecules. Experience with the corresponding DNA−DNA reaction shows that hybridizations on solid supports manifest rich phenomenology thermodynamically[11−25] and kinetically.[15,16,26−30] At the surface new variables emerge, including probe density[11,13,14,18,19,21,23,25,28,31−37] and surface potential,[12,30,38] that can strongly impact hybridization. Surface hybridization of even short oligomeric strands can proceed in multiple stages suggestive of sequential molecular rearrangements,[26−28,30] with the origins of this intriguing behavior still not well understood.[27,29] These complex characteristics limit predictive modeling, interfere with accurate interpretation of diagnostic results, and motivate basic research to connect organization of the surface with kinetic barriers and thermodynamic functions. The present study addresses key facets of this relationship for kinetics of hybridization between MO monolayers and comparably sized, complementary DNA targets.

Our analysis is based on real-time electrochemical quantification of unhybridized and hybridized surface sites that is used to directly correlate the instantaneous surface state with reaction rates. When applied to early stage hybridization, this analysis reveals important corrections analogous to those in sequential adsorption processes where previously bound molecules pose a barrier to later arrivals.[39,40] Incorporation of these corrections in a kinetic model together with description of the surface molecular packing leads to close agreement between experiment and model calculations. In comparison, the classic Langmuir model introduced in 1918 for gas adsorption,[41] and often used to interpret kinetics of surface hybridization reactions,[42−48]

Received: March 23, 2011
Published: June 23, 2011

Table 1. Morpholino and DNA Sequences

sequence	abbreviation	comments
5′ NH_2-TTT TAA ATT CTG CAA GTG AT-$CO(CH_2)_3SS(CH_2)_3CONH_2$ 3′	PM1	MO probe
5′ $HO(CH_2)_6SS(CH_2)_6$-ATC ACT TGC AGA ATT TAA 3′	TD1	complementary target to PM1[a]
5′ GAG GTT CAT GTT TGT GCC-$(CH_2)_3SS(CH_2)_3OH$ 3′	TP53	non-complementary control

[a] TD1 is complementary to the first 18 bases at the 3′ end of the PM1 probe.

produces equally good fits but only if certain physical constraints are relaxed, ultimately underscoring oversimplifications in its underlying assumptions. At higher duplex coverages MO−DNA surface hybridization exhibits additional, qualitatively different kinetic regimes. Possible origins of this more intricate behavior are discussed, and a comparison is carried out to available kinetic data for DNA and peptide nucleic acid probes in search for elements of universal behavior across different probe types.

2. MATERIALS AND METHODS

2.1. Materials. The morpholino probe sequence PM1 (Table 1) was taken from the retinoblastoma RB1 marker and was purchased from Gene Tools LLC (Philomath, OR). The 20mer probes were modified with a C3 disulfide at the 3′ end to allow for surface attachment to gold electrodes, and with a primary amine at the 5′ end to provide a bioconjugation site for ferrocenylformylglycine-NHS ester (FcFG-NHS), which served as an electroactive tag.[49] Complementary 18mer DNA targets TD1 and noncomplementary 18mer DNA controls TP53 (Table 1) were purchased from Integrated DNA Technologies (Coralville, IA). Both oligonucleotides contained a protected thiol in the form of a disulfide for conjugation to *N*-(2-ferrocene-ethyl) maleimide (FEM), with labeling performed as previously described.[18] The labeling protocol for FcFG-NHS was the same as that for the NHS ester of ferrocene carboxylic acid (FcCA-NHS) in ref 9. FcFG-NHS was used instead of FcCA-NHS because its longer linker arm increases labeling yields.[49] All ferrocene-modified MO and DNA molecules were purified by HPLC prior to use. Figure S1 in the Supporting Information depicts structures of the modified MO and DNA oligomers.

2.2. Preparation of Morpholino Monolayers. A 3 mm diameter, polycrystalline gold rotating disk electrode (RDE) served as the solid support. Prior to preparation of a probe layer the electrode was mechanically polished with a 1 μm diamond suspension (Bioanalytical Systems, West Lafayette, IN), rinsed with methanol and deionized water (18.2 MΩ cm resistivity), and electrochemically cleaned in 0.5 mol L^{-1} sulfuric acid with potentiodynamic cycling.[2] After a deionized water rinse, the roughness factor r_f (r_f = actual area/geometric area; $r_f \geq 1$) of the cleaned electrode was measured from the double-layer capacitance using previously described methods.[50,51] Values of r_f ranged from 1.41 to 1.88, with an average of 1.50 ± 0.16.

FcFG-labeled PM1 morpholinos were dissolved in deionized water to a concentration of 1.0, 2.0, or 4.0 μmol L^{-1}. Fifteen μL of the morpholino solution was deposited on freshly polished RDE electrodes for 30 min, followed by a deionized water rinse and immersion in 1 mmol L^{-1} blocking solution of 6-mercapto-1-hexanol (MCH; 97% purity) in deionized water for 2 h. The MCH passivation minimizes nonspecific adsorption of DNA targets and disrupts nonspecific contacts between MO probes and the electrode.[2] The change from mercaptopropanol as the passivant, used previously,[2,9] to MCH was motivated by improved stability of the thicker MCH monolayers to repeated potential scanning with cyclic voltammetry (CV) used for real-time monitoring of kinetics. This change also resulted in decreased hybridization yields, attributed to increased steric penalties from MCH interfering with base-pair formation at the one or two positions closest to the solid support, similar to observations for DNA probe films.[16] After a final rinse with deionized water, MO-modified electrodes were mounted on the RDE rotator and immersed in hybridization buffer containing 25 nmol L^{-1} target. The buffer was deoxygenated for at least 5 min prior to insertion of the RDE by nitrogen bubbling, and a nitrogen blanket was kept above the solution during measurements. To minimize possibility of contamination, electrodes were kept wetted by a droplet of the most recently applied solution during transfer steps.

2.3. Hybridization Measurements. Measurements were performed on an RDE rotator (Bioanalytical Systems) connected to a CHI660C electrochemical workstation (CH Instruments, Austin, TX). The sample cell contained the MO-modified and MCH-passivated 3 mm gold working electrode, a platinum wire counter electrode, and an Ag/AgCl/3 mol L^{-1} KCl reference electrode. All potentials are reported relative to this reference. Hybridizations were performed using 25 nmol L^{-1} FEM-labeled targets in pH 7.0 sodium phosphate at a concentration C_B of buffer phosphate groups of 0.01, 0.05, 0.1, or 0.5 mol L^{-1}. No other salt or buffer ingredients were present. Reverse, or dehybridization, reactions were performed by switching a hybridized probe layer into a target-free buffer of the same ionic strength. The RDE rotational speed was 1500 rpm.

The instantaneous target coverage S_D was determined from the total charge required to switch the oxidation state of the targets' FEM tags. This charge was measured with CV and was converted to molecular coverage following previously reported methods.[2] CV measurements were taken every 5 min at a scan rate of 5 V s^{-1}. Briefly, S_D follows from $S_D = Q_{FEM}/(eA_g r_f)$ where Q_{FEM} is total charge from conversion of the FEM oxidation state, e is elementary charge, and $A_g r_f$ is total electrode area given by product of the geometric area A_g and roughness factor r_f. The total probe coverage S_0 was similarly derived from redox switching of the probe FcFG tags. Here, $S_0 = S_D + S_P$ where S_P is coverage of unhybridized probes. Figure S2 in the Supporting Information shows a sample CV trace together with a computer-generated fit used to determine Q_{FEM} and Q_{FcFG}.

Control experiments confirmed that (1) the sampling frequency of one CV scan every 5 min was sufficiently low to avoid biasing of hybridization kinetics, and (2) the scan rate of 5 V s^{-1} was sufficiently slow to avoid signal attenuation due to electron transfer limitations. The first concern was addressed through measurements in which sampling times were varied from 10 to 600 s as hybridization progressed, and noting that for times of 2 min or longer there were no discernible changes in hybridization rates. The second issue was addressed by calculating probe coverages from CV voltammograms measured at sweep rates from 0.1 to 2000 V s^{-1} and noting that calculated coverages stabilized for 10 V s^{-1} and lower (Figure 1A). The need for slower sweep rates, compared to our earlier study which used 20 V s^{-1},[9] is attributed to a higher charge transfer barrier presented by the thicker MCH as opposed to mercaptopropanol passivation. When CV data were not being collected, the working electrode was held at 0 V.

2.4. Other Controls. Hybridization kinetics were analyzed under the assumption that mass transport resistance associated with delivery of targets to the probe layer was negligible. The significance of mass transport can be assessed using the Damköhler number $Da = k_F S_0/k_M$, where k_F is the forward hybridization rate constant and k_M is the mass transport coefficient.[28,52] For $Da \ll 1$, reaction kinetics are slower than

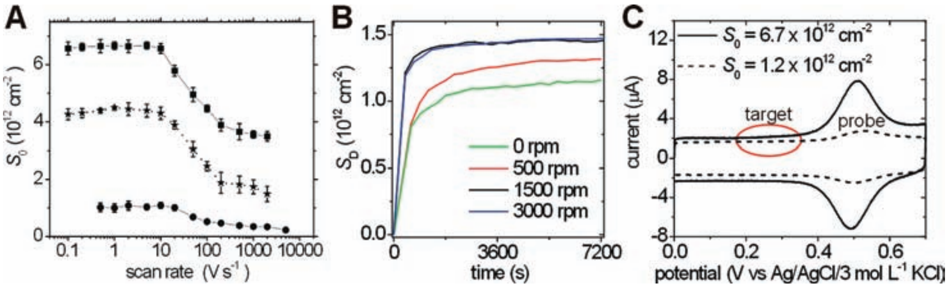

Figure 1. Examples of experimental controls. (A) Effect of CV scan rate on calculated coverages, for three different samples. (B) Effect of RDE rotational speed on hybridization under conditions of low reaction resistance, thus emphasizing mass transfer limitations (conditions: S_0 = (1.24 ± 0.07) × 10^{12} cm^{-2}; C_B = 0.5 mol L^{-1}; target concentration = 25 nmol L^{-1}). (C) CV traces after 5 h under 25 nmol L^{-1} non-complementry TP53 target in 0.1 mol L^{-1} buffer at the indicated probe coverages. The large peak close to 0.5 V corresponds to FcFG signal from PM1 probes. The FEM TP53 signal, if present, would lie between 0.25 and 0.3 V (circled area).

Table 2. Experimental Conditions and Derived Model Parameters[a]

S_0 ($\times 10^{12}$ cm^{-2})	C_B (mol L^{-1})	k_F ($\times 10^3$ L mol^{-1} s^{-1})[b]	Z_E (nm^2)[b]
1.20	0.010	15 ± 1	190 ± 3
3.5	0.010	1.4 ± 0.1	300 ± 8
6.1	0.010	0.86 ± 0.01	440 ± 9
1.8	0.050	18 ± 1	120 ± 2
4.0	0.050	2.8 ± 0.1	120 ± 3
6.2	0.050	4.0 ± 0.1	140 ± 2
1.4	0.10	100 ± 5	73 ± 1
3.8	0.10	14 ± 1	72 ± 1
6.6	0.10	6.6 ± 0.2	69 ± 1
1.4	0.50	320 ± 20	51 ± 1
3.0	0.50	27 ± 1	50 ± 1
6.4	0.50	27 ± 1	32 ± 1

[a] k_F and Z_E are defined in eq 6. The listed values are from fits to the first hour of hybridization. [b] Uncertainties represent standard error from fitting of eq 6 to data.

mass transport and therefore represent the dominant rate resistance; in this limit, mass transfer limitations can be neglected. To check consistency with this approximation, *Da* was estimated for experimentally derived k_F values as described in section S3 in the Supporting Information. Depending on S_0 and ionic strength, *Da* was found to range from 0.0035 to 0.18; therefore, kinetic limitations rather than mass transport were dominant. The highest value of 0.18 applied to lowest probe coverage S_0 and highest buffer concentration C_B, when hybridization rates were observed to be fastest. Even for these conditions, however, mass transport was not significant at the RDE rotational speed used, ω = 1500 rpm, since doubling ω had little, if any, effect (Figure 1B). Accordingly, data were interpreted purely from a reaction kinetic perspective, under assumption of negligible mass transport resistance.

Controls for nonspecific adsorption of targets used the TP53 sequence (Table 1) labeled with the FEM tag. Experiments were performed at high and low probe coverages, and various buffer concentrations. These measurements showed that nonspecific target adsorption was below quantification (Figure 1C). Therefore, nonspecific adsorption was treated as negligible and target signals were fully attributed to duplexes formed through sequence-specific base pairing.

3. RESULTS AND DISCUSSION

3.1. General Observations. Kinetic traces, consisting of the duplex coverage S_D as a function of time, were determined for four sodium phosphate buffer concentrations C_B (0.01, 0.05, 0.1, and 0.5 mol L^{-1}), with no other salt present, and three probe coverages S_0 (~ 1.5 × 10^{12}, ~ 3.5 × 10^{12}, and ~6 × 10^{12} cm^{-2}). Table 2 summarizes these conditions, with remaining entries discussed below. Hybridization was followed for 2 h, with a few runs performed for longer times. Figure 2A–C shows examples of data collected at the three coverages and at C_B = 0.1 mol L^{-1}. All coverages exhibit a gradual decrease in hybridization rate r = dS_D/dt over the initial hour, with the lowest coverage (Figure 2A) approaching saturation within this time. After this initial or "stage I" regime, the behavior often transitioned to an approximately linear increase in S_D with time. During this second stage, r was nearly constant, as indicated by the dashed lines in Figure 2A–C. That consumption of the probe reagent was not accompanied by slowing of the reaction is suggestive of an "autocatalytic" effect. Our inspection of published hybridization traces reveals that such behavior can also arise in hybridization to PNA probes (especially at lower ionic strengths)[53,54] and, at times, to DNA probes,[26,55] as well as in protein adsorption.[56] At even longer times (stage III in Figure 2D), the hybridization rate again starts to decrease with S_D in a protracted approach to equilibrium. Similar overall trends were observed when hybridization was carried out at C_B = 0.01 and 0.5 mol L^{-1} at the high probe coverage, for which longer runs were also performed. This evidence indicates that distinct kinetic mechanisms can become operative at different time points during MO–DNA surface hybridization.

Figure 3 illustrates that dehybridization, following placement of samples under target-free buffer, was very slow. This is indicated by stability of the target peak appearing at ~0.27 V and was true for all conditions of S_0 and C_B tested. The lack of dehybridization was an important constraint in the following kinetic analysis.

3.2. Stage I: Langmuir Analysis. Langmuir kinetics[41] have modeled both DNA–DNA[42–48,57] and PNA–DNA[45,53,54,58] surface hybridization and provide an appropriate starting point for considering the corresponding MO–DNA process. In the irreversible Langmuir model, the forward rate r_F of hybridization between targets T and probes P to form duplexes D, P + T → D, is proportional to frequency of P–T collisions, given by the product of the solution target concentration $C_{T,B}$ and the surface coverage of available probes S_P:

$$\frac{dS_D}{dt} = r_F = k_F C_{T,B} S_P = k_F C_{T,B}(S_0 - S_D) \qquad (1)$$

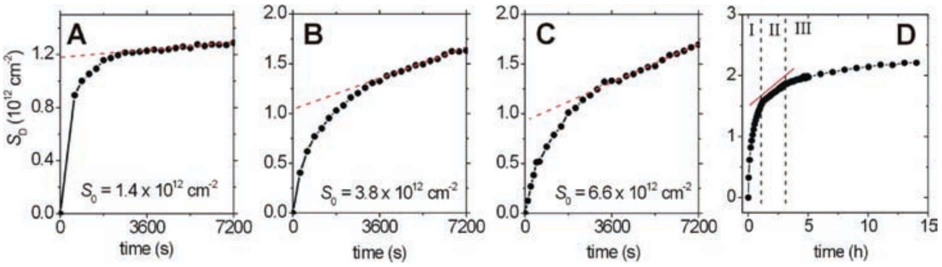

Figure 2. (A−C) Hybridization kinetics for $C_B = 0.1$ mol L^{-1} at three probe coverages S_0. (D) Long-term kinetic data for the experiment in part C. The trace can be divided into distinct regimes as discussed in the text. In all cases, red lines serve as visual guides to help judge linearity of S_D with time.

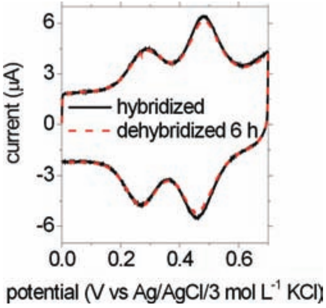

Figure 3. CVs illustrating lack of dehybridization after 6 h under a target-free buffer, following a 14 h hybridization run ($S_0 = 6.6 \times 10^{12}$ cm^{-2}, $C_B = 0.1$ mol L^{-1}). The peak around 0.27 V corresponds to the target FEM tags, while that around 0.47 V corresponds to the probe FcFG tags.

with k_F the forward rate constant. For reversible reactions, P + T ↔ D, a reverse rate r_R is added to represent dehybridization:

$$\frac{dS_D}{dt} = r_F - r_R = k_F C_{T,B}(S_0 - S_D) - k_R S_D \tag{2}$$

with k_R the reverse rate constant. k_F and k_R are expected to depend on all parameters that affect molecular interactions at the surface, including total probe coverage, surface potential, buffer composition, temperature, strand sequences, and the extent of hybridization. Although the extent of hybridization varies with time, the Langmuir model assumes that binding sites do not interact; this implies that k_F and k_R are independent of the state of surrounding sites and thus independent of S_D. Recalling that mass transport resistances were negligible (section 2.4), the time-integrated analytical forms of eqs 1 and 2 were used to directly fit stage I data during the first 60 min of hybridization.

Figure 4 illustrates Langmuir fits for $S_0 = 1.2 \times 10^{12}$ cm^{-2} and $C_B = 0.01$ mol L^{-1}. Assumption of irreversible kinetics according to eq 1, with k_F and S_0 treated as adjustable, led to good agreement, as shown by the black line in Figure 4; however, the derived $S_{0\mathrm{Fit}} = 4.8 \times 10^{11}$ cm^{-2} was significantly off the actual coverage $S_0 = 1.2 \times 10^{12}$ cm^{-2}. If, instead, $S_{0\mathrm{Fit}}$ was set equal to S_0 and only k_F was allowed to vary the agreement was poor (Figure 4, red line). Assumption of reversible kinetics as per eq 2 with the constraint $S_{0\mathrm{Fit}} = S_0$ and k_F and k_R as floating parameters recovered good agreement (Figure 4, green points). This fit, however, was again not physically meaningful because the derived k_R predicted significant dehybridization where little was observed experimentally. In summary, although Langmuir kinetics could produce numerically excellent fits, this was only possible by violating constraints on dehybridization rates or probe coverage. Therefore, an alternate kinetic model was sought that could simultaneously account for all experimental information.

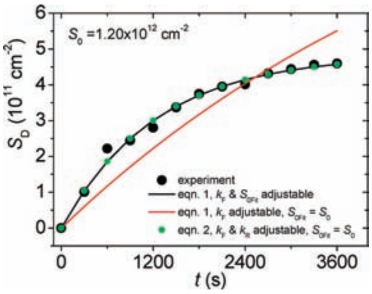

Figure 4. Comparison of fits based on Langmuir kinetics for $S_0 = 1.2 \times 10^{12}$ cm^{-2} and $C_B = 0.01$ mol L^{-1}. Black points, experimental data; black line, irreversible kinetics, eq 1, with k_F and $S_{0\mathrm{Fit}}$ as fit parameters ($k_F = 3.2 \times 10^4$ L mol^{-1} s^{-1}, $S_{0\mathrm{Fit}} = 4.8 \times 10^{11}$ cm^{-2}, $R^2 = 0.992$); red line, irreversible kinetics, eq 1, with k_F variable and $S_{0\mathrm{Fit}}$ constrained to $S_{0\mathrm{Fit}} = S_0 = 1.2 \times 10^{12}$ cm^{-2} ($k_F = 6.8 \times 10^3$ L mol^{-1} s^{-1}, $R^2 = 0.82$); green points, reversible kinetics, eq 2, with k_F and k_R variable and $S_{0\mathrm{Fit}}$ constrained to 1.2×10^{12} cm^{-2} ($k_F = 1.3 \times 10^4$ L mol^{-1} s^{-1}, $k_R = 4.8 \times 10^{-4}$ s^{-1}, $R^2 = 0.99$).

3.3. Stage I: An Experimentally Derived Kinetic Mechanism.

Rather than assume a particular kinetic model, one can ask what model features are suggested by experimental data. The reaction rate is taken to follow

$$\frac{dS_D}{dt} = k_F g(S_D) C_{T,B}(S_0 - S_D) \tag{3}$$

where dehybridization has been neglected because of the very slow off rates. Equation 3 abandons the assumption of site independence and recognizes that changes in layer structure with hybridization may alter reactivity of the probe layer. The impact of these changes is captured in the effective rate constant $k_F g(S_D)$, where S_D parametrizes the extent of hybridization and through the unknown function g alters the site reactivity. k_F now represents an "intrinsic" rate constant at the onset of hybridization, when $S_D = 0$ and $g = 1$. The dependence of g on S_D follows directly from eq 3:

$$k_F g(S_D) = \frac{1}{C_{T,B}(S_0 - S_D)} \frac{dS_D}{dt} \tag{4}$$

with all terms on the right side accessible from experiment. Because calculation of dS_D/dt required differentiation, to minimize introduction of numerical noise the data were first fit to an analytic function which was then differentiated. A Lorentz-type function was selected because it closely captured experimental $S_D(t)$ traces over the first hour and yet was unrelated to any

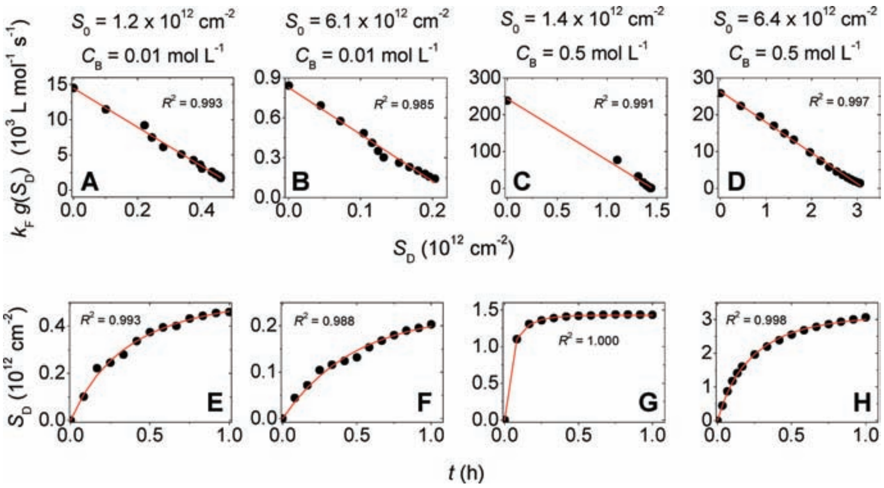

Figure 5. (A−D). Experimentally derived dependence of $k_F g(S_D)$ on S_D according to eq 4, for combinations of S_0 and C_B indicated at the top. Points are data, and lines are linear approximations. (E−H) Corresponding model fits. Points are data, and lines are fits based on eq 6.

expected form of the response. Examples of Lorentz fits at the four limits of probe coverage and ionic strength are shown in Figure S3 in the Supporting Information. Figure 5A−D shows the derived dependence of $k_F g$ on S_D as calculated from eq 4.

The results in Figure 5A−D suggest an approximately linear decrease of the effective rate constant $k_F g(S_D)$ with S_D. Therefore, stage I data were reanalyzed using $g = 1 - Z_E S_D$, corresponding to

$$\frac{dS_D}{dt} = k_F(1 - Z_E S_D)C_{T,B}(S_0 - S_D) \tag{5}$$

and the time-integrated form

$$S_D = k_F S_0 \frac{1 - \exp[C_{T,B} k_F t(1 - Z_E S_0)]}{k_F Z_E S_0 - k_F \exp[C_{T,B} k_F t(1 - Z_E S_0)]} \tag{6}$$

Equation 6 has two parameters, k_F and Z_E, whose optimized values are compiled for all conditions in Table 2. Examples of fits are shown in Figure 5E−H; these fits satisfy constraints of negligible off rates as well as pinning of S_0 at the experimental value, which could not be simultaneously met by Langmuir kinetics. Fits were also performed to just the first 30 min of hybridization to check whether the 60 min analysis was biased by overlap with stage II; the 30 and 60 min analyses yielded results that were identical within fitting uncertainties.

The good fit quality of eq 6 shows that a linear dependence of g on S_D successfully accounts for all experimental observations but does not clarify physical origins of this dependence. In contrast to DNA probes, unhybridized MO probes are expected to exist in a desolvated state due to their lower solubility, as schematically depicted in Figure 6A.[9] A desolvated organization of MO probes, of the same sequence as in this study, was previously deduced from electrochemical measurements of the interfacial capacitance of such films.[2,3] MO−DNA duplexes are expected to be more soluble because of their DNA charge, and in a mixed layer should therefore segregate toward the solution (Figure 6B).[3,9] The resultant stratification, in which duplexes protrude away from the surface, is expected to hinder hybridization because targets must first pass across the duplex layer before encountering an unhybridized probe. The dependence of g on the duplex coverage S_D presumably accounts for corrections due to this barrier.

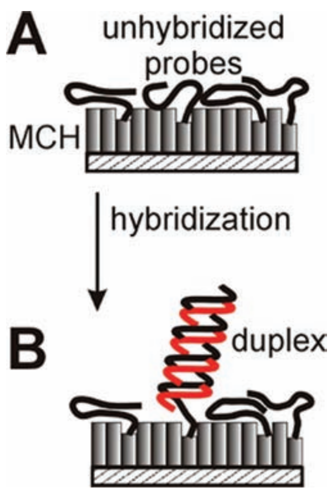

Figure 6. Schematic of (A) unhybridized and (B) partially hybridized MO layers. In (B), a stratified organization exists due to formation of more soluble MO−DNA duplexes that extend above the underlayer of less soluble, unhybridized probes.

The linear dependence of g on S_D indicates that each duplex contributes to the hybridization barrier independently; that is, corrections nonlinear in S_D, which would be expected once interactions between duplexes set in, are not yet significant. In this "linear" regime the parameter Z_E can be interpreted as an exclusion zone associated with a single duplex, with $Z_E S_D$ then the surface fraction inaccessible to targets due to occlusion by duplexes. The form of this correction, although derived directly from experiment, is consistent with theoretical expectations. For example, it is analogous to the first-order adjustment in the accessible surface fraction encountered in sequential adsorption processes (e.g., eq 18 in ref 39).

Z_E is expected to depend on ionic strength since both duplexes and targets are charged; therefore, the duplex−target interaction will have an electrostatic component. In contrast, it is not expected to depend strongly on coverage of unhybridized probes since there is no apparent mechanism through which the probes, collapsed on the solid support, could significantly influence the duplex−target interaction. Inspection of the Z_E values in Table 2

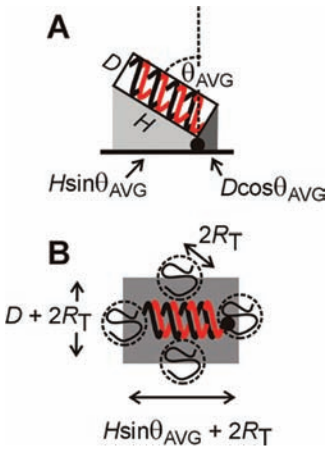

Figure 7. (A) Definition of duplex width D, length H, and average tilt angle θ_{AVG}. (B) The shaded region approximates the area excluded by a duplex to the center of mass of a target coil, where R_{T} is the target radius. The picture assumes $m = 0$ in eq 7.

largely confirms these expectations. The increased scatter at the lowest ionic strength of 0.01 mol L^{-1} is attributed to uncertainties in quantifying the rather small duplex coverages in this limit.

If the interpretation of Z_{E} as the area around a duplex from which targets are excluded is correct, it should be possible to relate it to the duplex and target molecular dimensions. As illustrated by the shaded region in Figure 7B, this area depends on the duplex width D and length H (Figure 7A), and the target radius R_{T}. If a duplex is on average tilted by an angle θ_{AVG} to the surface normal then, based purely on geometric considerations, the center of mass of a target coil would be excluded from an area $Z_{\mathrm{E,CAL}} \approx (D + 2R_{\mathrm{T}})(H \sin \theta_{\mathrm{AVG}} + 2R_{\mathrm{T}})$,[59] assuming $H \sin \theta_{\mathrm{AVG}} \gg D \cos \theta_{\mathrm{AVG}}$ in Figure 7A. The exclusion zone must in addition have an electrostatic component, the form of which is not known. However, since electrostatic interactions are exponentially screened over length scales comparable to the Debye length r_{D}, any additional separation imposed by electrostatics should be at most a few r_{D}. If m is the number of Debye lengths defining the target−duplex separation permitted by electrostatics, then the approximation for $Z_{\mathrm{E,CAL}}$ becomes

$$Z_{\mathrm{E,\,CAL}} \approx (D + 2R_{\mathrm{T}} + 2mr_{\mathrm{D}})(H \sin \theta_{\mathrm{AVG}} + 2R_{\mathrm{T}} + 2mr_{\mathrm{D}}) \tag{7}$$

For comparing experimental Z_{E} values with those calculated from eq 7, and in the absence of structural information on MO−DNA duplexes,[60] molecular dimensions were assumed to correspond to those of B-form DNA with $D = 2$ nm and $H = 5.8$ nm. Moreover, duplexes were assumed to behave as freely hinged rods subject only to impenetrability of the solid support; in this case a uniformly distributed θ_{AVG} evaluates to 57°. The assumption of freely hinged orientation rests on absence of significant duplex−duplex interactions, consistent with early stage hybridization, as well as unimportance of duplex−surface interactions. Hydrodynamic alignment of duplexes due to the RDE shear flow was also neglected. This last assumption can be checked through the dimensionless ratio γ/D_{ROT}, where γ is the local shear rate and D_{ROT} is the duplex rotational diffusion coefficient.[61,62] For our conditions $\gamma/D_{\mathrm{ROT}} < 1 \times 10^{-3}$ (section S5, Supporting Information); in this limit hydrodynamic alignment is not significant. The last input, R_{T}, was taken equal to the target radius of gyration, $R_{\mathrm{g}} = (l_{\mathrm{P}} L_{\mathrm{C}}/3)^{1/2}$, where $L_{\mathrm{C}} = N_{\mathrm{T}} l_{\mathrm{N}}$ is the contour length, $N_{\mathrm{T}} = 18$ is the number of nucleotides per target, $l_{\mathrm{N}} = 0.43$ nm is the length per nucleotide,[63] and $l_{\mathrm{P}} = c_0 + c_1/C_{\mathrm{Na,B}}{}^{1/2}$ is the persistence length of single-stranded DNA, with c_0 and c_1 taken from ref 64 and $C_{\mathrm{Na,B}}$ the solution cation concentration.

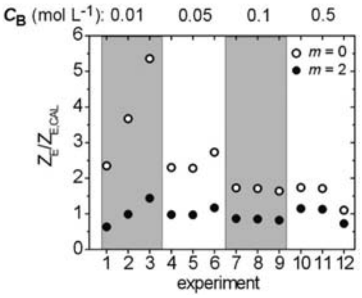

Figure 8. Ratio of measured (Z_{E}) to estimated ($Z_{\mathrm{E,CAL}}$) exclusion areas for the 12 experimental conditions listed in Table 2. Open circles: $Z_{\mathrm{E,CAL}}$ based on steric exclusion only; $m = 0$ in eq 7. Filled circles: $Z_{\mathrm{E,CAL}}$ based on combination of steric and electrostatic exclusion; $m = 2$ in eq 7. The experiments are listed by ionic strength, as indicated at top of the plot.

Figure 8 compares experimental Z_{E} to $Z_{\mathrm{E,CAL}}$ estimated from eq 7. For $m = 0$ (open circles, Figure 8) the ratio $Z_{\mathrm{E}}/Z_{\mathrm{E,CAL}}$ clusters around 2, a reasonable agreement given the approximate treatment; however, $Z_{\mathrm{E}}/Z_{\mathrm{E,CAL}}$ tends to decrease with ionic strength, suggesting that setting $m = 0$ underestimates the role of electrostatics. For $m = 0$, electrostatics enter solely through the target persistence length l_{P}. Setting $m = 2$ (filled circles, Figure 8) has the simultaneous effect of nearly eliminating variation of $Z_{\mathrm{E}}/Z_{\mathrm{E,CAL}}$ with ionic strength and of bringing predicted values close to experimental ones, so that $Z_{\mathrm{E}}/Z_{\mathrm{E,CAL}} \approx 1$. These improvements are consistent with the expected importance of electrostatics in the duplex−target interaction.

The second model parameter, k_{F}, represents the intrinsic reactivity of the probe layer in the limit $S_{\mathrm{D}} = 0$. From Table 2, a roughly 10-fold decrease in k_{F} occurs as probe coverage increases from ~1.5 × 10^{12} to ~3.5 × 10^{12} cm^{-2}. This decrease in k_{F} is attributed to increased stabilization of probes by probe−probe associations at higher S_0, since such aggregation presents an activation barrier to hybridization. The data in Table 2 moreover suggest this effect plateaus at higher coverages, perhaps because of diminished impact of coverage changes once the films become nearly continuous around $S_0 \approx 5 \times 10^{12}$ cm^{-2}.[3] A practical consequence of these observations is that faster response times should result if probe coverages are kept low.

Interestingly, k_{F} decreased approximately 20-fold when C_{B} was lowered from 0.5 to 0.01 mol L^{-1}, Table 2. This trend could in principle arise from charge on the solid support that is repulsive to the DNA target molecules. Although unhybridized MO probes are not charged, negative charge could reside on the metal electrode itself and increasingly oppose hybridization as ionic strength is lowered. Such an explanation, however, is inconsistent with MCH-passivated electrodes typically exhibiting negative potentials of zero charge (pzc),[65,66] what implies MCH supports to have a positive charge at the 0 V used for hybridization. Our own measurements, based on minimum in interfacial capacitance,[67] confirmed that pzc is negative for MCH-passivated electrodes bearing unhybridized MO probes under pH 7.0 sodium phosphate, with pzc falling between −0.1 and −0.2 V.[68]

Therefore, some other, as yet unidentified effect is believed responsible for the dependence of k_F on C_B. One such possibility arises from C_B-induced changes in target conformation. Kinetics of duplex formation might be favored, for example, by more compact target conformations, realized at higher C_B, that locally concentrate nucleotides to accelerate formation of stably base-paired MO−DNA nuclei.

In summary, the forward rate for stage I kinetics is found to obey

$$r_F = k_F(1 - Z_E S_D)(S_0 - S_D)C_{T,B} \tag{8}$$

Here, k_F represents intrinsic reactivity of the functionalized support, in the $S_D = 0$ limit, and depends on all parameters that affect the interaction of a target with the unhybridized probe film. The factor $1 - Z_E S_D$ accounts for steric and electrostatic occlusion of target access to unhybridized probes due to protrusion of previously formed duplexes normal to the support. The conventional term $S_0 - S_D$ enforces the upper limit $S_D = S_0$ and accounts for deactivation of the support due to consumption of probe segments by hybridization, what leaves fewer MO segments per area to nucleate duplex formation.[69] The last factor, $C_{T,B}$, is the usual impact of solution concentration on the frequency of hybridization attempts.

3.4. Comments on Later Kinetic Stages. The transitions to stage II and stage III behavior are not yet fully understood. Since during stage I interactions between duplexes are weak, one possible explanation for the stage I/II transition is that it coincides with onset of duplex−duplex interactions. Such interactions could cause duplexes to align, decreasing Z_E and thereby facilitating access to unhybridized probes. By offsetting deactivation of the solid support due to consumption of probes, the alignment could contribute to the near constancy in rate of hybridization observed during stage II. Interestingly, in protein adsorption, stage II like behavior has been attributed to conformational changes in which the occupied area per protein decreases as coverage increases;[56] this is analogous to the duplex reorientation mechanism proposed here.

Once duplexes become significantly aligned, the hybridization rate would be expected to again decrease with S_D as indeed observed in stage III. If this interpretation is correct, then according to Figure 2D a modest increase in S_D during stage II (e.g., by about 20% from 1.6×10^{12} to 1.9×10^{12} cm^{-2} in Figure 2D) should trigger significant alignment. These coverages correspond to interduplex distances of 7−8 nm and are thus well within contact range, as would be required. Also, as recently discussed,[9] in this last stage approach to equilibrium is expected to become especially hindered once dimensions of the voids between duplexes fall below those of average target conformations, thereby forcing targets to adopt significantly distorted, and hence rarer, conformations in order to reach an unhybridized probe. These more complex kinetic behaviors can be avoided by restricting duplex coverages to remain in stage I (e.g., by keeping the total probe coverage S_0 modest), what should simplify analysis of surface hybridization data based on MO probes.

3.5. Comparison of MO−DNA, DNA−DNA, and PNA−DNA Surface Hybridization Kinetics. Direct comparison of different probe systems at present is challenged by variations in surface chemistry, experimental conditions, and data interpretation methods between studies. Even for the most investigated scenario, that of DNA−DNA surface hybridization, some studies find Langmuir kinetics a reasonable approximation[42−48,57,70] while others find richer behavior with multiple stages or time scales,[15,16,26−30] reminiscent of the multiple stages in MO−DNA hybridization. Based on studies with model oligonucleotide systems, behavior closer to Langmuir kinetics appears to result when DNA probe lengths are kept below 20mers[42−45,47,48] and the probes are not too close together.[15]

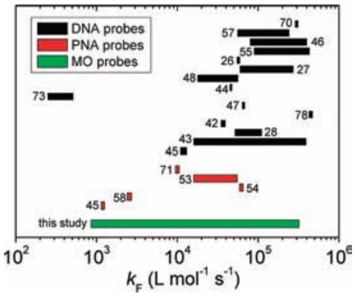

Figure 9. Compilation of forward rate constants k_F for noncompetitive surface hybridization of complementary targets to DNA, PNA, and MO probes. Numbers next to each entry cite the original study.

When more intricate behavior with multiple stages is observed, it may not necessarily reflect correspondence of underlying mechanisms and, indeed, we are not aware of our explanations for MO probe systems being applied in situations when DNA probes are used.[27,30] However, kinetic mechanisms for the two cases should become similar if a DNA probe layer stratifies into an underlayer of unhybridized probes and an overlayer of DNA−DNA duplexes. This situation could arise, for example, from adsorption of the unhybridized probes to the support, thereby producing similarity in layer organization and hybridization mechanisms to the MO system. In one study[34] where DNA probes adsorbed to the solid support predictions of Langmuir kinetics were especially far from experimental observations and the hybridization trace (Figure 3 in ref 34) exhibited similarity to Figure 2D.

Most studies of surface hybridization to PNA probes have employed shorter assay times, 10 min or less,[45,53,58,71] precluding comparison with long-term trends. When times of up to 2 h were considered deviations from Langmuir kinetics became apparent that bear resemblance to regime I/II behavior, especially at lower ionic strengths (e.g., Figure 2 in ref 54 and Figure 5 in ref 53). Like MOs, PNAs are uncharged and even less soluble;[8] therefore, it seems plausible that surface organization of PNA probes may be similar to that of MO probes, with unhybridized PNA near the solid support. Similarity in kinetic mechanisms would then be expected as, in order to hybridize, targets would have to again traverse the barrier presented by the duplex layer. This expectation could be further examined by testing PNA probes over a similar range of conditions as for MO probes.

Figure 9 compiles literature values of rate constants k_F for the three probe systems. All of the data are for oligomer-sized, 10mer to 30mer, probes hybridizing to fully complementary, comparable length DNA targets under noncompetitive conditions (i.e., no other target sequences are present). On the right side of the plot the rates approach 10^6 L mol^{-1} s^{-1}. This limit can be compared to solution rates which, for hybridization of DNA oligonucleotides, fall between 10^5 to 10^7 L mol^{-1} s^{-1}.[72] The upper k_F limit, therefore, appears to approach solution values. While both DNA and MO probes demonstrate reactivities close to this limit, such performance is only realized under favorable conditions. As discussed in section 3.3 and Table 2, MO probes hybridized fastest at low coverages and high ionic strengths. Probe coverage is also crucial for kinetics of DNA−DNA surface hybridization;[32] indeed, two of the fastest rates in Figure 9 were for probe coverages below 1×10^{12} cm^{-2}.[46,55]

Interestingly, DNA probes generally do not yield k_F values less than 10^4 L mol^{-1} s^{-1}, with the one exception the study by Sekar et al.[73] In contrast, MO and PNA probes exhibit values down to $\sim 10^3$ L mol^{-1} s^{-1}. As discussed in section 3.3, the slow limit for MO probes arises under high coverages at which these probes are expected to aggregate, thus creating an activation barrier to hybridization. Keeping probe coverages modest can avoid this slowdown. However, it is important to recognize that the postulated benefits of reduced probe coverage are based on results from noncompetitive hybridization and may not directly extrapolate to multiplexed hybridization as practiced in microarrays. Multiplexed experiments must also contend with cross-reactions in which partly matched targets occupy the probes and interfere with binding of the perfect match;[74−76] these cross-reactions, whose impact depends on rates of dehybridization of the partial matches, may be a more significant kinetic obstacle to buildup of the sequence-specific signal than probe−probe interactions. Temperature, not considered as a variable in the present study, also becomes critical to optimization of multiplexed assays.[77]

4. CONCLUSIONS

Hybridization between oligomer morpholino probes and complementary DNA targets exhibits a rich kinetic behavior that, in general, defies explanation by a single mechanism. The intrinsic reactivity of the unhybridized probe layer depends on both probe coverage and ionic strength, with fastest kinetics observed at low probe coverages and high ionic strengths. The dependence on probe coverage is attributed to lessened association between probes at low coverages; that on ionic strength is not yet understood. As hybridization proceeds, distinct kinetic stages appear, and the rate of hybridization exhibits dependency on the extent of hybridization not captured by classical Langmuir kinetics. These observations are consistent with an interfacial organization in which unhybridized probes segregate near the solid support, while hybridized duplexes segregate to the solution side. The resultant stratification subjects later-arriving targets to a barrier imposed by the growing duplex layer. During the first stage of hybridization, duplexes contribute independently to this barrier through exclusion of targets from a zone around each duplex. At higher duplex coverages, an unusual regime can arise in which the hybridization rate becomes nearly independent of the extent of hybridization, followed by a third stage in which the rate again decreases with duplex coverage. One possible explanation for the second stage is that it reflects the onset of duplex−duplex interactions that, temporarily, can be relaxed by duplex alignment to maintain the hybridization rate approximately constant; once this degree of freedom is exhausted, further hybridization becomes more and more kinetically attenuated as the duplex layer continues to fill in.

Comparison with literature data reveals that MO probes exhibit reactivities that span the full range observed with DNA and PNA probes, and that approach solution rates under favorable conditions. These comparisons are also supportive of the notion that different probe types exhibit comparable kinetic mechanisms if their interfacial organization is similar; however, available data sets are limited, and more systematic studies, across multiple probe types and under similar experimental conditions, are needed to fully explore this issue.

■ ASSOCIATED CONTENT

Ⓢ **Supporting Information.** Molecular structures of FcFG-PM1 and FEM-TD1, summary of CV curve analysis for determining probe and duplex coverages, estimation of *Da* numbers, examples of fits used for differentiation of data in eq 4, and discussion of hydrodynamic effects on duplex alignment. This material is available free of charge via the Internet at http://pubs.acs.org.

■ AUTHOR INFORMATION

Corresponding Author

rlevicky@poly.edu

■ ACKNOWLEDGMENT

This project was supported by Award No. R01HG004512 from the National Human Genome Research Institute and by Awards No. DMR 07-06170 and DGE 07-41714 from the National Science Foundation.

■ REFERENCES

(1) Summerton, J.; Weller, D. *Antisense Nucleic Acids* **1997**, *7*, 187.

(2) Tercero, N.; Wang, K.; Gong, P.; Levicky, R. *J. Am. Chem. Soc.* **2009**, *131*, 4953.

(3) Tercero, N.; Wang, K.; Levicky, R. *Langmuir* **2010**, *26*, 14351.

(4) Wang, X.; Smirnov, S. *ACS Nano* **2009**, *3*, 1004.

(5) Gao, Z.; Ting, B. P. *Analyst* **2009**, *134*, 952.

(6) Li, S. J.; Li, J.; Wang, K.; Wang, C.; Xu, J. J.; Chen, H. Y.; Xia, X. H.; Huo, Q. *ACS Nano* **2010**, *4*, 6417.

(7) Zhang, G. J.; Luo, Z. H.; Huang, M. J.; Tay, G. K.; Lim, E. J. *Biosens. Bioelectron.* **2010**, *25*, 2447.

(8) Summerton, J. E. *Lett. Pept. Sci.* **2004**, *10*, 215.

(9) Gong, P.; Wang, K.; Liu, Y.; Shepard, K.; Levicky, R. *J. Am. Chem. Soc.* **2010**, *132*, 9663.

(10) Müller, H.-J.; Röder, T. *Microarrays*; Elsevier Academic Press: Burlington, MA, 2006.

(11) Vainrub, A.; Pettitt, B. M. *Phys. Rev. E* **2002**, *66*, 041905.

(12) Vainrub, A.; Pettitt, B. M. *Biopolymers* **2003**, *68*, 265.

(13) Halperin, A.; Buhot, A.; Zhulina, E. B. *Biophys. J.* **2004**, *86*, 718.

(14) Halperin, A.; Buhot, A.; Zhulina, E. B. *J. Phys.: Condens. Mat.* **2006**, *18*, S463.

(15) Peterson, A. W.; Wolf, L. K.; Georgiadis, R. M. *J. Am. Chem. Soc.* **2002**, *124*, 14601.

(16) Wong, E. L. S.; Chow, E.; Gooding, J. J. *Langmuir* **2005**, *21*, 6957.

(17) Fiche, J. B.; Buhot, A.; Calemczuk, R.; Livache, T. *Biophys. J.* **2007**, *92*, 935.

(18) Gong, P.; Levicky, R. *Proc. Natl. Acad. Sci. U.S.A.* **2008**, *105*, 5301.

(19) Irving, D.; Gong, P.; Levicky, R. *J. Phys. Chem. B.* **2010**, *114*, 7631.

(20) Fuchs, J.; Fiche, J. B.; Buhot, A.; Calemczuk, R.; Livache, T. *Biophys. J.* **2010**, *99*, 1886.

(21) Stachowiak, J. C.; Yue, M.; Castelino, K.; Chakraborty, A.; Majumdar, A. *Langmuir* **2006**, *22*, 263.

(22) Hagan, M. F.; Majumdar, A.; Chakraborty, A. K. *J. Phys. Chem. B* **2002**, *106*, 10163.

(23) Gong, P.; Lee, C.-Y.; Gamble, L. J.; Castner, D. G.; Grainger, D. W. *Anal. Chem.* **2006**, *78*, 3326.

(24) Jayaraman, A.; Hall, C. K.; Genzer, J. *Biophys. J.* **2006**, *91*, 2227.

(25) Jayaraman, A.; Hall, C. K.; Genzer, J. *J. Chem. Phys.* **2007**, *127*, 144912.

(26) Gao, Y.; Wolf, L. K.; Georgiadis, R. M. *Nucleic Acids Res.* **2006**, *34*, 3370.

(27) Glazer, M.; Fidanza, J. A.; McGall, G. H.; Trulson, M. O.; Forman, J. E.; Suseno, A.; Frank, C. W. *Anal. Biochem.* **2006**, *358*, 225.

(28) Henry, M. R.; Stevens, P. W.; Sun, J.; Kelso, D. M. *Anal. Biochem.* **1999**, *276*, 204.

(29) Hooyberghs, J.; Baiesi, M.; Ferrantini, A.; Carlon, E. *Phys. Rev. E* **2010**, *81*, 012901.

(30) Su, H.-J.; Surrey, S.; McKenzie, S. E.; Fortina, P.; Graves, D. J. *Electrophoresis* **2002**, *23*, 1551.

(31) Halperin, A.; Buhot, A.; Zhulina, E. *Langmuir* **2006**, *22*, 11290.

(32) Peterson, A. W.; Heaton, R. J.; Georgiadis, R. M. *Nucleic Acids Res.* **2001**, *29*, 5163.

(33) Steel, A. B.; Herne, T. M.; Tarlov, M. J. *Anal. Chem.* **1998**, *70*, 4670.

(34) Zeng, J.; Almadidy, A.; Watterson, J.; Krull, U. K. *Sens. Actuators B* **2003**, *90*, 68.

(35) Hagan, M. F.; Chakraborty, A. K. *J. Chem. Phys.* **2004**, *120*, 4958.

(36) Lee, C. Y.; Nguyen, P. C. T.; Grainger, D. W.; Gamble, L. J.; Castner, D. G. *Anal. Chem.* **2007**, *79*, 4390.

(37) Shen, G.; Anand, M. F. G.; Levicky, R. *Nucleic Acids Res.* **2004**, *32*, 5973.

(38) Heaton, R. J.; Peterson, A. W.; Georgiadis, R. M. *Proc. Natl. Acad. Sci. U.S.A.* **2001**, *98*, 3701.

(39) Schaaf, P.; Talbot, J. *Phys. Rev. Lett.* **1989**, *62*, 175.

(40) Talbot, J.; Tarjus, G.; Van Tassel, P. R.; Viot, P. *Colloids Surf. A—Physicochem. Eng. Asp.* **2000**, *165*, 287.

(41) Langmuir, I. *J. Am. Chem. Soc.* **1918**, *40*, 1361.

(42) Liebermann, T.; Knoll, W.; Sluka, P.; Herrmann, R. *Colloids Surf. A* **2000**, *169*, 337.

(43) Okahata, Y.; Kawase, M.; Niikura, K.; Ohtake, F.; Furusawa, H.; Ebara, Y. *Anal. Chem.* **1998**, *70*, 1288.

(44) Zhang, Z.; Knoll, W.; Foerch, R.; Holcomb, R.; Roitman, D. *Macromolecules* **2005**, *38*, 1271.

(45) Jensen, K. K.; Orum, H.; Nielsen, P. E.; Norden, B. *Biochemistry* **1997**, *36*, 5072.

(46) Mocanu, D.; Kolesnychenko, A.; Aarts, S.; Dejong, A. T.; Pierik, A.; Coene, W.; Vossenaar, E.; Stapert, H. *Anal. Biochem.* **2008**, *380*, 84.

(47) Yu, F.; Yao, D.; Knoll, W. *Nucleic Acids Res.* **2004**, *32*, e75.

(48) Tawa, K.; Yao, D. F.; Knoll, W. *Biosens. Bioelectron.* **2005**, *21*, 322.

(49) Ge, D.; Levicky, R. *Chem. Commun.* **2010**, *46*, 7190.

(50) Oesch, U.; Janata, J. *Electrochim. Acta* **1983**, *28*, 1237.

(51) Shen, G.; Tercero, N.; Gaspar, M. A.; Varughese, B.; Shepard, K.; Levicky, R. *J. Am. Chem. Soc.* **2006**, *128*, 8427.

(52) Dandy, D. S.; Wu, P.; Grainger, D. W. *Proc. Natl. Acad. Sci. U.S.A.* **2007**, *104*, 8223.

(53) Park, H.; Germini, A.; Sforza, S.; Corradini, R.; Marchelli, R.; Knoll, W. *Biointerphases* **2007**, *2*, 80.

(54) Liu, J. Y.; Tian, S. J.; Nielsen, P. E.; Knoll, W. *Chem. Commun.* **2005**, 2969.

(55) Michel, W.; Mai, T.; Naiser, T.; Ott, A. *Biophys. J.* **2007**, *92*, 999.

(56) Schmitt, Y.; Hahl, H.; Gilow, C.; Mantz, H.; Jacobs, K.; Leidinger, O.; Bellion, M.; Santen, L. *Biomicrofluidics* **2010**, *4*, 032201.

(57) Xu, F.; Pellino, A. M.; Knoll, W. *Thin Solid Films* **2008**, *516*, 8634.

(58) Sato, Y.; Fujimoto, K.; Kawaguchi, H. *Colloids Surf. B:Biointerfaces* **2003**, *27*, 23.

(59) In reality duplexes exhibit a range of tilt angles θ, allowing for the possibility that a target fits "under" a duplex for sufficiently small θ. Such corrections are neglected within the present approximate treatment.

(60) Moulton, J. D.; Yan, Y.-L. *Curr. Protein Mol. Biol.* **2008**, *26*, 1.

(61) Hinch, E. J.; Leal, L. G. *J. Fluid Mech.* **1972**, *52*, 683.

(62) Doi, M.; Edwards, S. F. *The Theory of Polymer Dynamics*; Oxford University Press: New York, 1986.

(63) Record, M. T.; Anderson, C. F.; Lohman, T. M. *Q. Rev. Biophys.* **1978**, *11*, 103.

(64) Tinland, B.; Pluen, A.; Sturm, J.; Weill, G. *Macromolecules* **1997**, *30*, 5763.

(65) Rant, U.; Arinaga, K.; Fujita, S.; Yokoyama, N.; Abstreiter, G.; Tornow, M. *Org. Biomol. Chem.* **2006**, *4*, 3448.

(66) Rentsch, S.; Siegenthaler, H.; Papastavrou, G. *Langmuir* **2007**, *23*, 9083.

(67) Bard, A. J.; Faulkner, L. R. *Electrochemical Methods: Fundamentals and Applications*; 2nd ed.; Wiley & Sons, Inc.: New York, 2000.

(68) The reported pzc values for mercaptoalcohol monolayers vary widely. For example, pzc for mercaptopropanol was reported to be around 0.05 V (O'Connor; et al. *ECS Trans.* **2011**, *35*, 99), and that for mercaptoundecanol around 0.03 V,[66] both slightly positive, while mercaptohexanol and mercaptohexadecanol yielded negative values at −0.23 and −0.13 V, respectively.[66] The values from ref 66 have been expressed vs Ag/AgCl/3 mol L^{-1} NaCl. O'Connor et al. used 0.2 M sodium phosphate pH 7.0 buffer as electrolyte, while ref 66 used 0.1 mM KCl at a pH of 4.7.

(69) As S_D increases, the area left for unhybridized probes may also decrease, thus concentrating their segments and partially compensating for deactivation due to probe consumption. This correction was not applied, as it was not necessary to explain the experimental data.

(70) Yu, Y. M.; Feng, C. L.; Caminade, A. M.; Majoral, J. P.; Knoll, W. *Langmuir* **2009**, *25*, 13680.

(71) Uno, T.; Tabata, H.; Kawai, T. *Anal. Chem.* **2007**, *79*, 52.

(72) Bloomfield, V. A.; Crothers, D. M.; Tinoco, I., Jr. *Nucleic Acids—Structures, Properties, and Functions*; University Science Books: Sausalito, CA, 2000.

(73) Sekar, M. M. A.; Bloch, W.; St John, P. M. *Nucleic Acids Res.* **2005**, *33*, 366.

(74) Bhanot, G.; Louzoun, Y.; Zhu, J.; DeLisi, C. *Biophys. J.* **2003**, *84*, 124.

(75) Bishop, J.; Wilson, C.; Chagovetz, A. M.; Blair, S. *Biophys. J.* **2007**, *92*, L10.

(76) Dai, H.; Meyer, M.; Stepaniants, S.; Ziman, M.; Stoughton, R. *Nucleic Acids Res.* **2002**, *30*, e86.

(77) Relogio, A.; Schwager, C.; Richter, A.; Ansorge, W.; Valcarcel, J. *Nucleic Acids Res.* **2002**, *30*, e51.

(78) Lehr, H.-P.; Reimann, M.; Brandenburg, A.; Sulz, G.; Klapproth, H. *Anal. Chem.* **2003**, *75*, 2414.